Giant, 18, 2024, 100282

Full-length article

Machine learning assisted design and optimization of plate-lattice structures with superior specific recovery force

Amir Teimouri, Adithya Challapalli, John Konlan, Guoqiang Li*

Department of Mechanical and Industrial Engineering, Louisiana State University, Baton Rouge, LA 70803, USA

Keywords: **Metamaterials, Plate-lattice structures, Conditional generative adversarial networks, Machine learning, Shape memory polymer**

In load carrying structures and devices, there is a growing need for shape memory polymer (SMP) metamaterials that are lightweight and have superior strength, remarkable flexibility, and substantial specific recovery force (SFR). One of the challenges is to find optimum lightweight structures with high SFR. To address this challenge, we propose a novel inverse design framework to design plate-lattice structures (PLSs) with user-defined optimum specific maximum compression strength. Consisting of three sub-frameworks, the performance of the inverse design framework was validated before it was utilized to optimize PLSs. The optimum PLSs developed are fabricated with 3D printing using a novel SMP. In addition, we have printed a solid cylinder and Cubic+Octet (control) PLSs to compare their structural capacity with the predicted structures. The optimized PLSs display 30 ~ 170 % greater SFR compared to the control PLS and solid cylinder. These findings suggest a promising strategy for enhancing the effectiveness of actuators based on SMP mechanical metamaterials. The inverse design framework has the potential to be utilized for generating structures with user-defined optimum mechanical properties.

1 Introduction

In recent years, 4D printing has emerged as a revolutionary technology in the realm of manufacturing [1,2]. Unlike traditional 3D printing, which focuses on creating parts with permanent shapes, 4D printing adds an extra dimension of time, enabling printed structures to transform and adapt to their environment with time. This transformative capability is achieved through the integration of shape memory polymers (SMPs) as inks. While other stimuli-responsive polymers respond to stimuli like light [3], electricity [4], or magnetic fields [5], SMPs are distinguished by their reversible shape transformations primarily induced by temperature shifts, typically the glass-transition temperature [6,7].

The shape memory effect in polymers opens up a myriad of possibilities for applications in self-healing [8], biomedical devices [9], aerospace engineering [10], soft robotics [11], tissue regeneration [12], artificial muscles [13], sealant [14], and loss circulation materials [15]. However, achieving efficient and reliable shape recovery remains a critical challenge. Enhancing shape recovery in polymers is a key area of research to fully harness the potential of shape memory materials. In addition to the remarkable shape recovery capabilities of 4D printed SMP structures, the importance of force recovery is becoming more evident for certain applications. One notable area is the development of adaptive structures, where SMPs with high

* Corresponding author.
E-mail address: lguoqi1@lsu.edu (G. Li).
Received 7 March 2024; Received in revised form 2 May 2024; Accepted 2 May 2024

 https://doi.org/10.1016/j.giant.2024.100282

force recovery are employed to enhance structural integrity and responsiveness [16]. Moreover, SMPs with high force recovery have been utilized in fields such as aerospace, robotics, medical devices, and wearable technology [17–19]. Recovery force in a specific SMP is solely determined by the programmed strain, since factors like rubbery modulus, shape recovery ratio, and shape fixity ratio are usually considered to be specific to the SMP itself. In simpler terms, greater displacement during programming results in increased strain, which in turn leads to higher energy storage and improved recovery force.

Common knowledge suggests that when a material is shaped into different structures such as I-beams, lattices, honeycombs, or auxetic structures instead of a solid cube or beam, its ability to carry loads can be substantially improved [20]. Likewise, there is an expectation that employing 3D printing for the fabrication of metamaterials from shape memory polymers (SMPs) could lead to an enhancement in the specific recovery force (SFR) when compared to solid SMP structures. One of the famous classes of artificial structures is the truss lattice structure. Previously, we designed biomimetic lattice structures with enhanced resistance to buckling [21]. The octet-truss structure is widely regarded as the most superior lattice in terms of mechanical properties among various truss lattices [22]. However, it is still not considered the optimal choice. Even though lattice structures have been the primary choice in mechanical metamaterials for the last twenty years, their performance is restricted due to poor structural efficiency. Another type of lattice structure is known as "Shellular," which combines the terms "shell" and "cellular". In this particular structure, the cells are made up of seamless and smoothly curved shells [23]. While shellular structures possess notable mathematical significance, they often fail to meet the performance requirements expected for load-bearing structures.

Plate-lattice structures (PLS), a type of mechanical metamaterial inspired by the closed-cell structures found in nature, have been increasingly garnering attention within the field of mechanical engineering. These materials are composed of plates that utilize material constraints in two directions [24]. During investigations into pure stiffness optimization, Sigmund et al. [25] made a noteworthy observation that optimal structures such as truss-like structures tend to be close-walled rather than open-walled. This study indicates that a closed box with a microstructure consisting of thin walls displayed a significantly higher stiffness, around 2-3 times greater, compared to an open cell structure featuring 12 trusses positioned along the edges of a cube with a low volume fraction. Furthermore, Liu et al. [26] used an analytical method to show that the stiffness of a cubic plate is two times higher than the stiffness of a cubic truss of the same mass. In any given loading direction, plate-lattices exhibit superior structural efficiency, meaning they distribute strain energy more evenly among their components and have a greater proportion of members aligned favorably with the loading direction, in contrast to a corresponding beam-lattice [27]. Therefore, the findings suggest that further investigation is warranted for the PLS. Nevertheless, these benefits are offset by a substantial rise in fabrication complexity. The closed-cell structures of three-dimensional plate lattices render traditional fabrication methods, such as assembly techniques unfeasible, leaving additive manufacturing as the sole viable approach. However, extracting raw materials contained within the closed cells remains a difficult task [24]. Furthermore, while PLS exhibits high stiffness, it does not ensure high recovery force if the material used is an SMP. As discussed above, a high recovery force is required for some applications. Hence, these structures should be studied further to address this problem.

Various methods have been employed in the literature to optimize metamaterials due to the wide range of parameters that can affect their properties [28–30]. A combination of homogenization schemes and genetic algorithms has been utilized in inverse engineering of metamaterials to identify architectures beyond orthotropy [31]. Also, the topology optimization method has been used to investigate acoustic metamaterials [32]. This technique discovered a subwavelength bandgap that inhibits the propagation of low-frequency sounds. In multiple investigations, finite element method (FEM) has been employed as a common technique to generate data for the optimization of lattice structures, composites, and metamaterials [33–35]. As a case in point, FEM analysis has been applied to study two-dimensional auxetic lattice structures. This investigation leveraged the shape memory effect inherent in the constituent material to predict both the in-plane modulus and Poisson's ratio of the structure [36]. Optimization techniques commonly employed in engineering design are often characterized by their time-consuming nature, sensitivity to initial and boundary conditions, and constraints imposed by limited design parameters. However, the integration of machine learning (ML) methods and conditional generative adversarial networks (CGANs) provides a promising avenue to expedite the design process and facilitate the discovery of structures with user-defined and optimum properties.

ML is a field of artificial intelligence where algorithms enable computers to learn from data and make predictions or perform tasks without explicit programming. In optimization, ML algorithms can efficiently search through a vast design space, predict performance metrics, and guide the exploration of promising solutions, leading to improved efficiency and effectiveness in solving optimization problems. One common approach is to use machine learning algorithms, such as neural networks, to establish a mapping between the design parameters and the desired properties or performance metrics of various structures [37-40]. A machine learning-based model has been developed to find the optimum parameters affecting stiffness and forward/backward snapping force of curved beams [41]. A new 3D-printed unit cell has been devised with maximum elastic modulus and minimum wave speed inside the structure, using convolutional neural networks [42]. In a recent study in our group, a unique framework consisting of a Generative Adversarial Network (GAN) and a machine learning regression model has been developed to discover thin-walled structures with high-stress recovery [43]. Growth-based cellular metamaterials have been optimized based on their star-shaped distances using an inverse machine learning framework [44]. The proposed framework for inverse design encompasses a wide range of achievable anisotropic stiffness properties. In earlier findings, we documented the discovery of several innovative lightweight metamaterials that

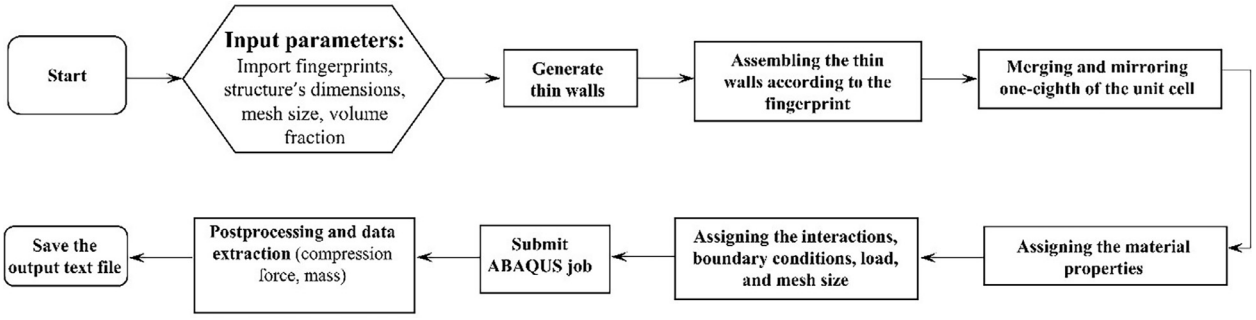

Fig. 1

Schematic of the workflow of the Python script used to simulate PLSs.

exhibit enhanced impact energy absorption capabilities, increased natural frequencies, and exceptional compression strengths, buckling loads [39,45,46]. However, few structures have been studied regarding shape recovery properties in mechanical metamaterials in the literature.

This paper introduces a novel inverse design framework containing a deep neural network (DNN) model and CGANs, which aims to identify orthotropic PLSs with user-defined and optimum mechanical properties for the first time. Two samples with user-defined properties are generated to validate the accuracy of the framework. Note that the recovery force depends on both the structural design and the SMP itself. While many efforts have been made to enhance the recovery force of SMPs, such as using enthalpy increase during programming as a mechanism of energy storage [47], this study focuses on structural design. Specifically, all the designed PLSs are made of the same SMP. Furthermore, FEM has been used to simulate the mechanical behavior of PLSs and generate data for training the framework. Optimum PLSs have been additively manufactured by a DLP (Digital Light Processing) printer to validate numerical simulations and to study force recovery properties. Several significant fabrication hurdles have been successfully addressed, including the elimination of surplus raw material pockets. The inverse design framework has the capacity to be employed in optimizing a broad spectrum of designs and uses in the realm of structural engineering.

2 Materials and methods

2.1 Automated simulations

FEM using Abaqus has been utilized in this investigation to simulate PLSs. The aim of this numerical analysis is to prepare a training dataset for machine learning, obtaining parameters such as geometrical parameters, fingerprints, the specific maximum compression force (SMCF), and the mass of the model. The novel method for fingerprinting each PLS will be explained in detail in Section 2.2. The amount of data plays a crucial role in machine learning as it directly impacts the model's performance and generalization ability. As the quantity of independent variables affecting outcomes grows, the required data size for efficiently training a model also expands in correlation with the escalation of independent variables. In this study, 2000 randomly generated fingerprints using the Mersenne Twister Algorithm [48] have been obtained as an input file to a novel Python script to generate, submit, and post-process each PLS to print the calculated maximum compressive force and mass in an output file. Afterward, The SMCF of each structure is calculated using the obtained data. The script for all finite element models is generated using Python version 3.10.0 and then processed using Abaqus version 2022 for computation. The schematic of this script is indicated in Fig. 1.

The overall ability of a structure to recover its original shape depends on two main factors: the shape recovery ratio of the SMP used, and the structural configuration. For given SMPs, their recovery force is influenced by the amount of strain they experienced during the programming phase. The term "programming phase" refers to the process in which the shape memory polymer (SMP) undergoes thermomechanical cycles to establish its temporary shape, which can later recover upon exposure to specific stimuli such as heat. In this study, the programming phase includes heating up the SMP structure above the glass transition temperature, applying pre-strain, cooling to below the glass transition temperature while holding the pre-strain constant, and unloading accompanied by a small springback.

Moreover, the design of the structure can indeed be a key parameter in determining the recovery force of a shape memory polymer. When the SMP is restrained to recover its original shape, the stored strain energy enables it to exert a stronger recovery force. While the recovery force is influenced by the amount of strain the SMP experienced during the programming phase, the structure into which the SMP is formed can affect how that strain is distributed and the efficiency of the shape recovery. The geometry of the structure can influence the distribution of strain and the overall recovery force. More complex structures may experience different stress and strain patterns during deformation and recovery. Since the programming phase of the structures in the experimental section is in the elastic range, in this investigation, PLSs undergo a fixed strain of 5 % to discover the PLS designs that have higher compressive force in this range of deformation. Consequently, during the simulations, the SMCF of the PLSs has been recorded.

To ensure reliable and consistent results, a mesh convergence analysis has been performed and the mesh size is configured to be 1.2mm. The numerical analysis concentrates exclusively on the elastic properties of the shape memory polymer (SMP) material. This approach is adopted to streamline the process and save time, avoiding the complexities that would arise from incorporating

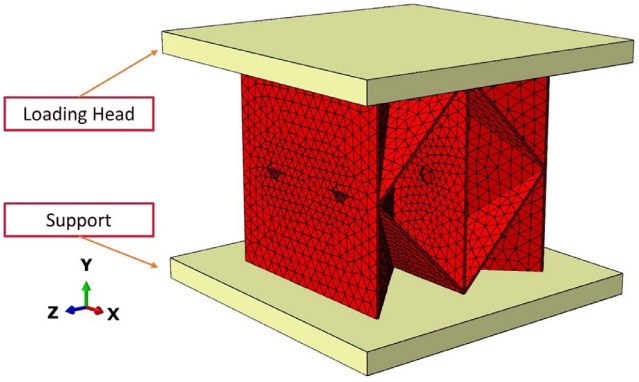

Fig. 2

The initial configuration before the simulation process, highlighting the geometric details of the structural model.

viscoelastic properties into the analysis. This is a reasonable assumption because if the PLS is programmed and recovered at rubbery state, the SMP can be treated as an elastic material. By excluding the viscoelastic aspects, the analysis becomes more efficient and less time-consuming, while still providing valuable insights into the behavior of the material under study. However, we must admit that polymers, including 3D printable polymers, are viscoelastic. Therefore, a more in-depth study should consider the nonlinear viscoelastic or even plastic behavior of the SMPs [49–52].

To calculate the elastic modulus of the polymer for simulations, experimental tests have been conducted based on the ASTM D695 standard test [53]. All the models are provided with an elastic material characterized by Young's modulus of 375 MPa and a Poisson's ratio of 0.4. Simulations are done through dynamic implicit analysis and PLSs are modeled using 4-node linear tetrahedron (C3D4) elements. Additionally, the load is applied by providing a 5 % strain in the vertical direction (Y-direction) to the loading head. A single support and one loading head are characterized as perfectly rigid cubic bodies measuring 30 by 30 by 2mm in size as presented in Fig. 2. Normal contact behavior is implemented between the PLS and the load cells using a rigid contact formulation. This choice ensures that no penetration occurs between the contacting surfaces, mimicking a rigid interaction. For tangential behavior, a penalty friction formulation with a friction coefficient of 0.3 is specified. This coefficient value represents the frictional resistance between the load cell and PLS surfaces in contact. By specifying this value, we aimed to simulate the frictional effects present in the experimental setup accurately. Additionally, due to the complexity of the model and the presence of several walls in the structure, the general contact feature has been implemented in the model. The model's dimensions match those of the experimental tests. The workstation boasts an i7 processor with 32 GB of RAM. It requires approximately 84 man-hours to complete the computational tasks for the training dataset, which encompass tasks such as generating models in Abaqus, submitting jobs, and post-processing.

2.2 Dataset generation and fingerprinting for PLSs

DNN is a powerful technique in predicting the output, based on given input parameters. Based on the number of independent variables affecting the output, the number of required training data changes. DNNs need a larger training dataset as the number of independent variables increases. To effectively train a DNN, a training dataset should be supplied, comprising both the inputs (structures) and the corresponding outputs (intended mechanical characteristics of each PLS). In order for the DNN to understand the PLSs, the structures need to undergo fingerprinting. Fingerprinting involves the conversion of each PLS into a digital sequence or pattern of numbers that can be read by a machine. In this section, we delineate the approach utilized to create our dataset aimed at predicting the mechanical properties of PLSs.

In the proposed structure, there are 20 types of walls with different orientations. Each of these walls has a specific position in the fingerprint array. In this research, every structure is initially identified by using the amalgamation of all the walls that constitute one-eighth of a representative volume element (RVE). A fingerprint comprises a sequence of 20 binary digits (e.g., "11100011000100010010") that denote the presence of walls within a PLS. Since the position of the walls in the RVE remains fixed, every PLS can possess a distinct and unique fingerprint. In Fig. 3 (a), a number has been assigned to each corner of the RVE to facilitate the fingerprinting process. Furthermore, Table 1 indicates the code of the walls and their corresponding positions in the fingerprint. Walls identified by four-digit codes represent quadrilateral structures, while three-digit codes correspond to triangular walls. For example, with the fingerprint "10100000000100010000", we can locate the corresponding unit cell depicted in Fig. 3(b). As depicted in Fig. 3(b), walls with codes 1526, 8473, 5643, and 163 are present in one-eighth of this PLS. These codes dictate the establishment of a wall between designated corners, with the associated binary digits in the fingerprint set to '1,' while the remaining digits should remain '0'. The process of converting any structure into a fingerprint, and *vice versa*, can be readily followed.

Table 1

Coding scheme for walls and their positions in the fingerprint.

Wall	Position	Wall	Position	Wall	Position	Wall	Position	Wall	Position
1526	1	5867	2	8473	3	1423	4	2367	5
1548	6	1537	7	1467	8	5823	9	4826	10
1287	11	5643	12	527	13	427	14	836	15
163	16	183	17	186	18	542	19	547	20

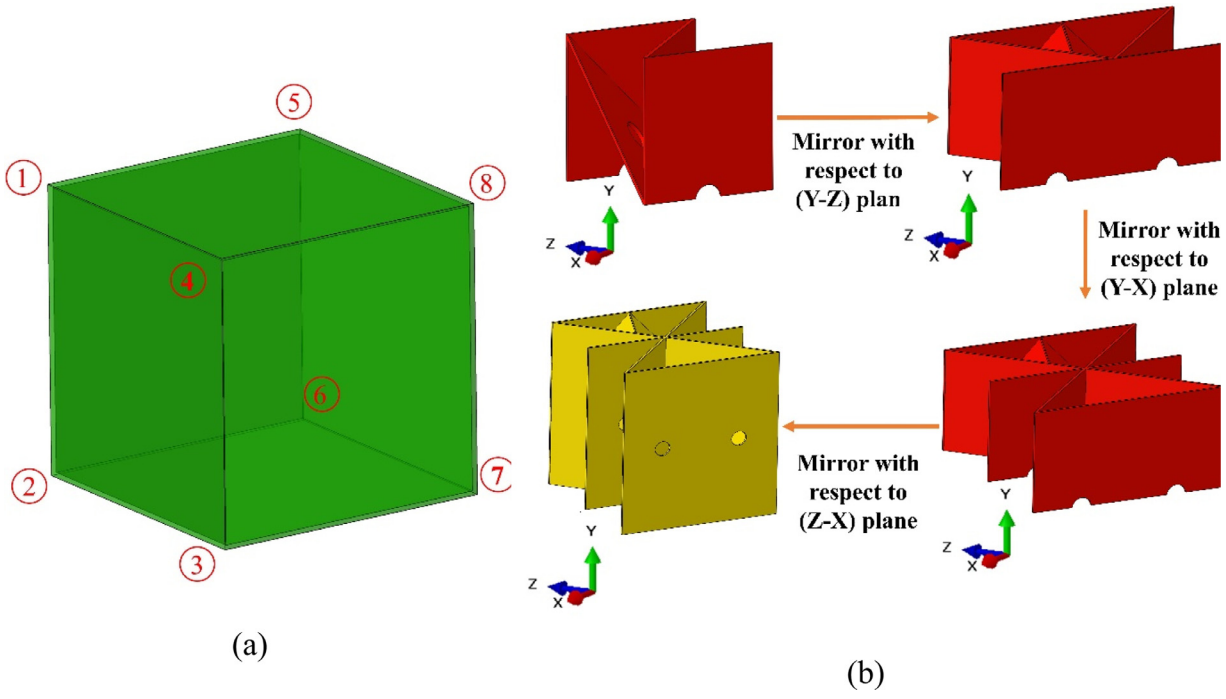

Fig. 3

The process of creating a PLS, based on a unique fingerprint. a) indicates the code corresponding to one-eighth of an RVE. b) Represents the process of mirroring a unit cell ("10100000000100010000") to create a full RVE.

After one-eighth of the RVE is ready, it must be mirrored with respect to various directions of the 3D coordinate system. The mirroring process and the final RVE with the fingerprint "10100000000100010000" can be seen in Fig. 3(b). Using this method, about one million PLSs can be generated (See **Fig. S1** for sample structures and their respective fingerprints). Using the Mersenne Twister Algorithm in Python, 2000 fingerprints were generated randomly considering the boundary conditions. While some combination of walls results in structures that are not interconnected, specific boundary conditions have been considered in the generation of fingerprints. Consequently, the generated fingerprints were given to the Python script as a text file to generate the PLS models in Abaqus. The closed-cell structures found in PLSs render traditional fabrication methods, such as assembly techniques, unfeasible, necessitating AM as the sole viable approach. However, the extraction of raw materials from within these enclosed cells poses a persistent challenge. To address this issue, small holes with a 1 mm diameter are incorporated on the surfaces of the plates, which enables the elimination of the unpolymerized resin after the printing process, even in the presence of a closed-cell topology. The position of these holes is fixed on each plate, so they are not included in the fingerprinting process.

2.3 DNN prediction

To improve the recovery force of PLSs, structures should have high stiffness in the rubbery state. One of the goals of this study is to find optimum PLSs with high SFR. Due to the substantial size of the dataset involved in this investigation, experimental and numerical analysis of each structure is an expensive and time-consuming project. The experimental process includes creating the structure, setting up the experiments, and conducting thermomechanical tests. This can be very time-consuming, especially when dealing with multiple samples. On the other hand, numerical analysis can be quite intricate due to the involvement of thermomechanical features, and non-linear material properties. Consequently, a DNN has been developed to predict the SMCF of each PLS. The schematic of the DNN has been presented in Fig. 4. Fingerprints are given as the input parameters to the network and their corresponding SMCF is the output of the network. The details for the DNN model's specifications are outlined in **Table S1**.

The DNN architecture was constructed using the Keras library [54], with sequential layers consisting of dense units. Several activation functions were examined to train the model and finally, the ReLu function was selected due to the enhanced level of accuracy. The input features were processed and normalized using the MinMaxScaler from the sci-kit-learn library to ensure consistent scaling across the dataset. The dataset was then divided into training (85 %) and testing (15 %) sets for model evaluation.

To facilitate the learning process, the DNN model utilized the mean absolute error (MAE) loss function and the Adam optimizer with a learning rate of 0.0001. The model was trained over 800 epochs with a batch size of 64, enabling it to capture complex relationships within the data and optimize the prediction accuracy. The performance of the DNN is assessed using the testing set throughout the entire training process, which consists of 800 epochs of updating the network weights. Fig. 5 **(a)** indicates that the MAE is decreased from 48.045 % and 50.96 % to 0.29 % and 1.41 % in training and testing sets, respectively. After

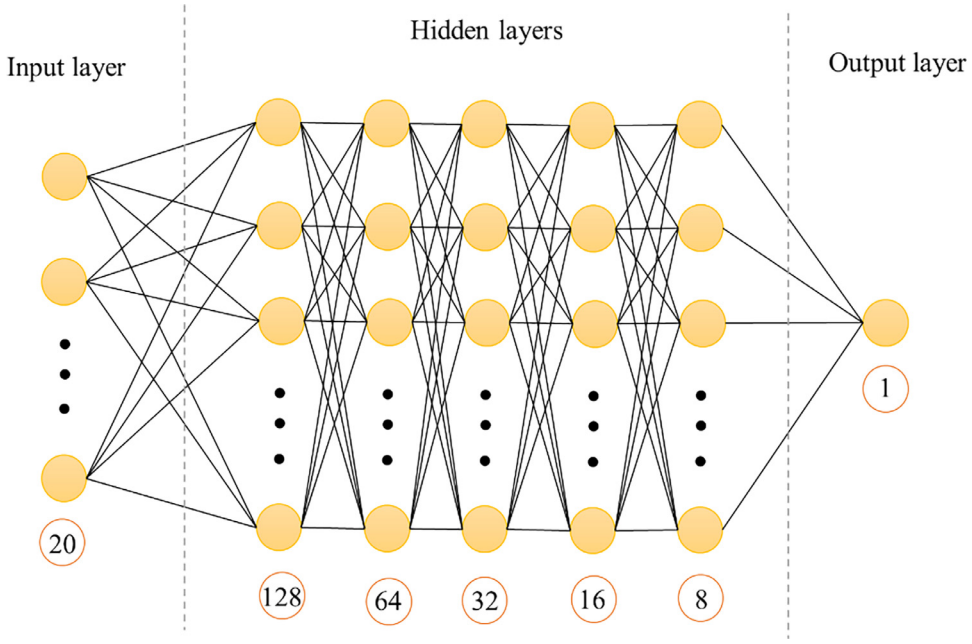

Fig. 4

The schematic of the DNN used for predicting the SMCF of each structure.

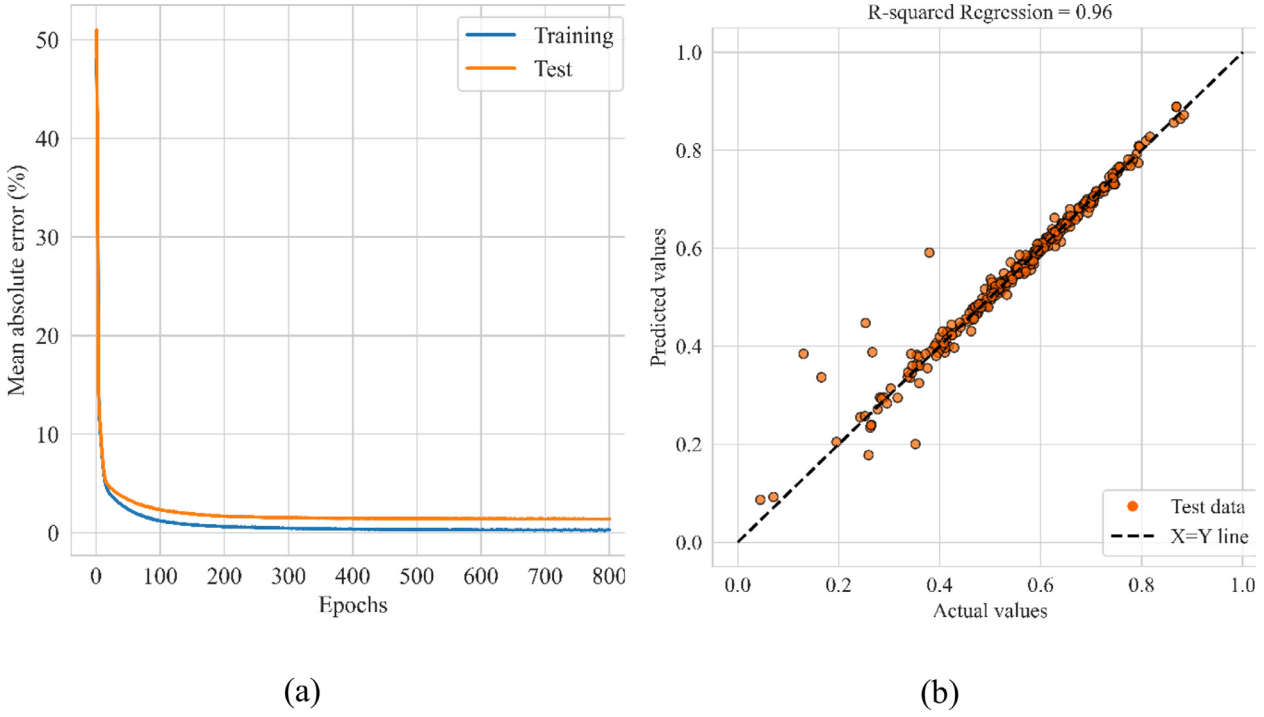

Fig. 5

(a) MAE (%) evolution over 800 epochs of training, assessed on training and testing sets. (b) R-squared plot for SMCF showcasing the correlation between mechanical properties of the PLSs using the DNN.

approximately 400 epochs, as depicted in Fig. 5**a**, the error plot reaches a plateau, indicating convergence of the model's training process. Despite this stabilization, we continued training up to 800 epochs to ensure the convergence is stable. This extended training duration allowed for thorough exploration of the model's performance beyond convergence with minimal time investment.

The model was evaluated using an R-squared score. Fig. 5**(b)** displays the regression plot for SMCF, showcasing a R-squared value of 0.96**.** The SMCF regression plot shows the relationship between predicted and actual values, with a well-fitted model displaying a tight cluster of points along a diagonal line. This DNN model offers a promising approach for predicting the SMCF

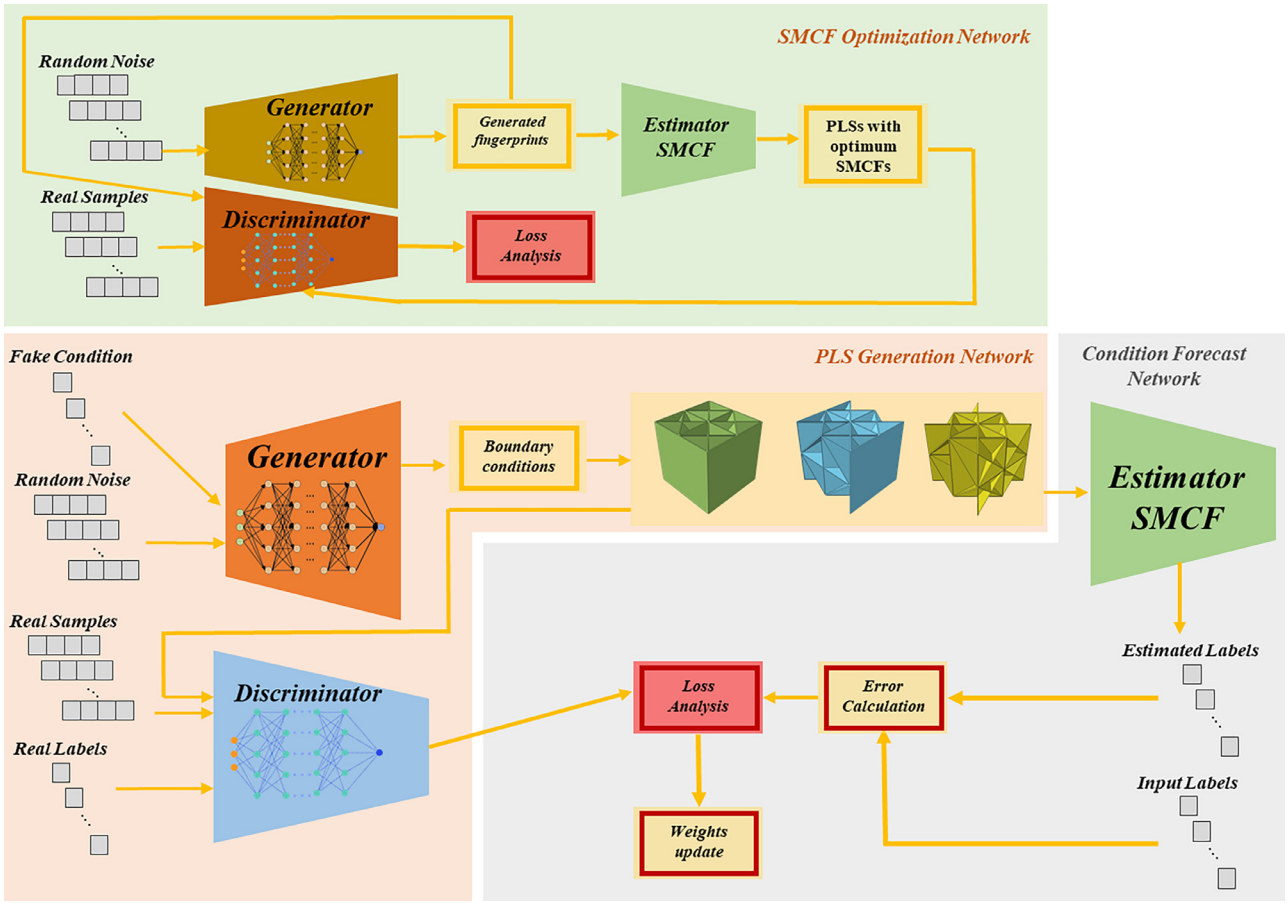

Fig. 6

The schematic of the inverse design framework for generating PLSs with user-defined and superior SMCF.

of PLSs, providing valuable insights for engineering applications and decision-making processes.

2.4 Inverse design using CGANs

The goal of this framework is to find structures with user-defined mechanical properties and, the structures with superior SMCF. Inverse design presents an innovative approach aimed at achieving a fundamental goal: crafting structures tailored to specific mechanical properties designated by the user. Since the number of structures in this study is very high, which makes the optimization process complicated for conventional methods such as genetic algorithms, topology optimization, etc., a novel inverse design framework has been developed to simplify the process of reaching the user-defined properties. Previously, Challapalli et al. [43] designed a framework to optimize thin-walled structures using GANs. They improved the specific recovery stress of a thin-walled structure by 50 % as compared with a honeycomb unit cell. Furthermore, CGANS has been used to predict the geometrical pattern of auxetic metamaterials with user-defined mechanical properties [35]. Uniaxial compression test and FEM have been used to validate their inverse design framework.

CGANs are a class of deep learning models that combine the power of generative models with the ability to control their output. They introduce a conditional component, allowing users to specify desired attributes or characteristics for the generated samples. The framework consists of a PLS generation network (PGN), a condition forecast network (CFN), and a SMCF optimization network (SON) (Fig. 6). In PGN, the generator aims to produce authentic fingerprints that match the specified conditions (user defined SMCF), while the discriminator learns to distinguish between real and fake fingerprints and the condition of each fingerprint. In this study, the term "real fingerprint" means a fingerprint that not only consists of 20 binary digits like the input fingerprints but also has a SMCF close to the user-defined input. The generator is trained iteratively alongside the discriminator in an adversarial manner. During each training epoch, the discriminator is first trained using a batch of real structural fingerprints paired with their corresponding mechanical properties, including normalized SMCF. Simultaneously, the generator produces synthetic structural fingerprints based on random noise inputs and randomly generated mechanical property conditions falling within predefined ranges. The generator's objective is to deceive the discriminator by producing synthetic fingerprints that are indistinguishable from real ones, effectively matching the desired mechanical properties specified by the user. To achieve this, the generator adjusts its parameters based on the feedback from the discriminator, striving to generate increasingly

accurate fingerprints corresponding to the desired mechanical properties.

Afterward, the CFN uses the trained DNN in the previous section to predict the SMCF of the generated fingerprints in PGN to estimate error and update weights. Moreover, the SON screens out the PLSs with superior SMCF using the trained DNN.

2.5 Performance of the inverse design framework

Evaluating the accuracy of the framework poses a formidable challenge due to its inherent complexity. Traditional evaluation metrics like accuracy, often used for classifiers, are ill-suited for CGANs. Metrics such as Inception Score and Frechet Inception Distance attempt to capture the quality and diversity of generated samples but are not without limitations [55]. In this study, we employed several methodologies to assess the efficacy of the inverse design framework. Firstly, the MAE calculation was employed as a pivotal metric. Throughout the training epochs, synthetic structural fingerprints were generated by the CGAN, accompanied by randomly assigned input conditions. The DNN predicts the corresponding normalized SMCF for each fingerprint, and the MAE was computed as the absolute difference between the output of the DNN and the predetermined input target. This approach facilitated a relative assessment of deviation, providing insights into the model's performance in generating structural designs aligned with specified mechanical property targets. Fig. 7 **(a)** indicates the Binary Cross Entropy Loss of the generator and discriminator along with MAE between the output of the SMCF estimator and the input target. MAE stabilized around 7 % after around 300 epochs. The generator and discriminator's specifications are presented in **Table S2** (Model 4).

Moreover, to assess the performance of the framework at various input conditions, 120 normalized values between 0 and 1 were selected uniformly and used to generate 500 fingerprints for each value. The average of the MAE between the target values and the SMCF of the generated fingerprints is illustrated in Fig. 7 **(b)**. At lower SMCFs within the design space, MAE fluctuates considerably between about 9 % and 4.5 %, but in input conditions above $1200\frac{N}{g/cm^3}$ the MAE stabilizes around 6.5%. The fluctuation in MAE at lower input conditions could be attributed to the unequal distribution or disparity within the training dataset. Nonetheless, across all input conditions, the average MAE remains stable at 6.72±0.23%, showcasing the technical viability of generating a collection of efficient PLSs for exploring further mechanical properties.

Additionally, 1000 labels were selected from the available input condition space and compared with their corresponding output labels generated by the DNN model. Illustrated in Fig. 7 **(c)**, the input values are represented on the horizontal axis while the output values are on the vertical axis. The proximity of points to the reference line X=Y indicates the degree to which the output labels align with our input labels.

Two samples were selected for FEM validation of the inverse design framework (Fig. 8). The framework was provided with the desired SMCF, yielding a fingerprint with properties that closely match the user-defined value. The fingerprint is then used to generate and simulate the corresponding PLS based on the explained process in Table 1 and Fig.1. The minimal discrepancies (3.05 % in sample 1 and 0.1 % in sample 2) observed between the target SMCF and the simulated output values demonstrate the remarkable precision of the inverse design framework in generating PLSs with user-defined properties.

2.6 PLS optimization process

For the optimization process, the CGAN converted to a GAN to develop a generator which is able to generate PLSs with superior SMCF. The GAN only needs random noise for the training process and the input conditions are eliminated. Firstly, we conducted an analysis involving the generation of 2000 unique fingerprints, serving as a benchmark to evaluate the diversity and uniqueness of the data synthesized by the GANs. This is a crucial aspect to ensure that the model is not only producing accurate samples but also a wide variety of them. To enhance the uniqueness of the generated fingerprints, we systematically varied the number of neurons and the activation function of each layer in both the generator and discriminator components of the GAN architecture. Through an iterative process, we aimed to identify the optimal configuration that maximizes the production of distinct fingerprints. Fig. 9 **(a)** elucidates the number of unique fingerprints generated by five models. The details for each model's specifications are outlined in **Table S2**. Taking into account the epoch count, the time duration for each training epoch, and the quantity of distinct fingerprints, Model-4 is chosen to proceed with the ongoing process. After approximately 500 epochs, Model-4 can produce fingerprints with a uniqueness of about 87.5 %.

The optimization is done in an iterative process. In the first iteration, the GAN is given 10000 unique fingerprints to be trained and generate new fingerprints. Then, the SMCF of each new fingerprint is predicted using the estimator. Fingerprints are sorted in terms of the SMCF and for the next iteration top fingerprints with higher MCF are given to the framework. In every iteration, the average normalized SMCF of the generated fingerprints is calculated and illustrated in Fig. 9 **(b).**

This plot indicates that the average normalized SMCF of fingerprints increases gradually through 25 iterations and reaches a plateau. After 25 iterations the average normalized SMCF of the PLSs increased by 61.8 %. This number in the final iterations is nearly approaching "1", suggesting that some of the generated structures outperform the PLSs present in the input data. The top 10 % of fingerprints in each iteration were saved and compared with the other iterations. The top fingerprints in the last five iterations were approximately the same which indicates that the optimization algorithm has converged. Furthermore. The top fingerprints of the last iteration are selected for further investigations.

The design criterion in this optimization is to find orthotropic structures with superior SMCF within the vast design space. Following the abovementioned steps, finally, PLSs with the following fingerprints are selected as the top three superior structures, respectively: 11110000001100100100 (Best-1), 11110000001100010101 (Best-2), 11010000001100110000 (Best-Iso). From this point in the article onwards, these structures are mentioned using their summarized name as Best-1, Best-2, and Best-Iso. Best-1 and Best-2 are the best orthotropic structures regarding SMCF and Best-Iso is the best

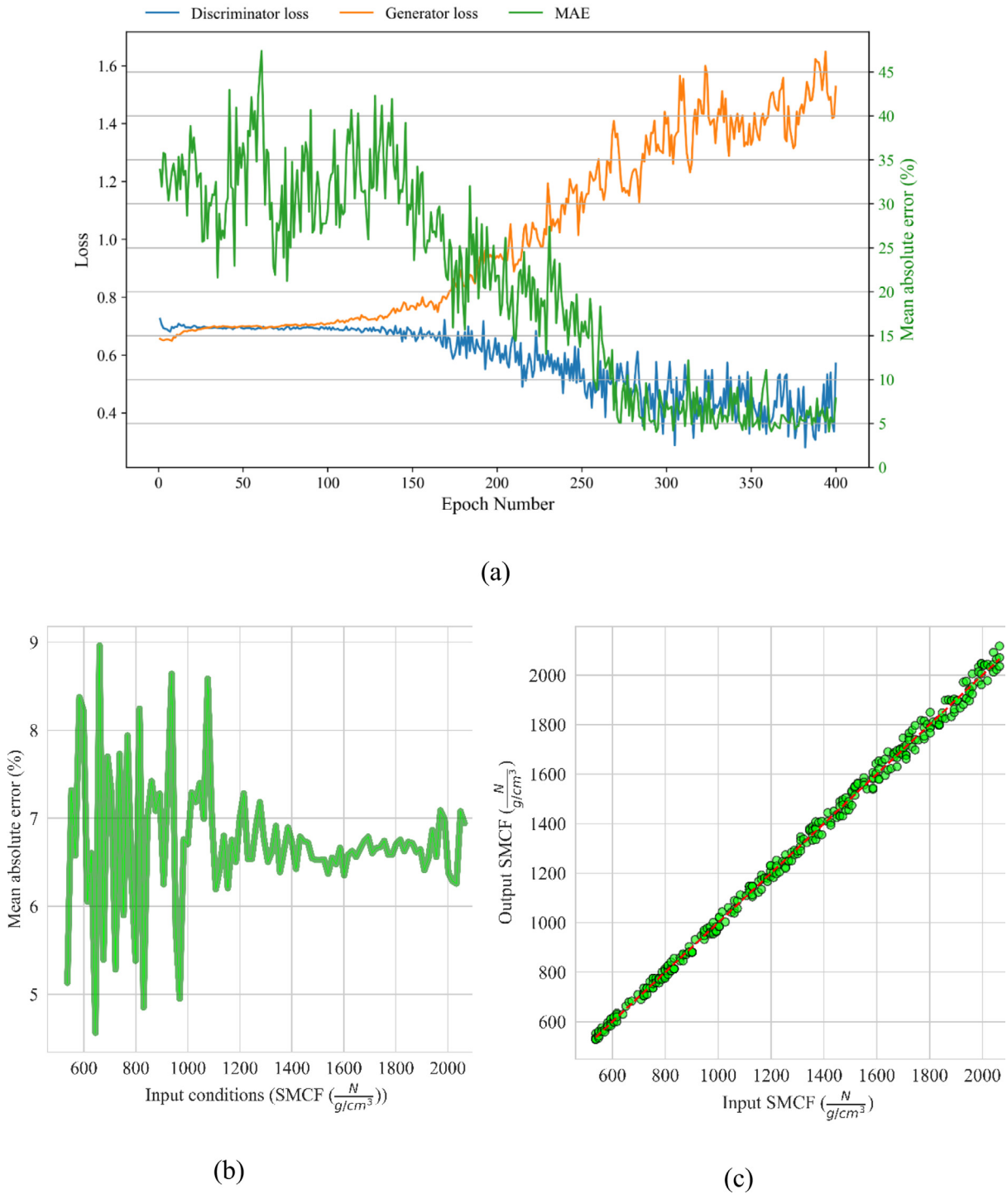

Fig. 7

(a) Training progression of the CGAN, showcasing discriminator and generator losses alongside MAE (%) evolution over 400 epochs. (b) Variation of MAE (%) of the CGAN across different input conditions, indicating model performance for predicting SMCF. (c) Comparison between output and desired SMCF values generated by the framework.

isotropic structure. To demonstrate the performance of the PLSs, they have been compared to the Cubic+Octet structure (11001000000000111100), recognized as a superior PLS in literature [24]. Henceforth, the Cubic+Octet PLS will be denoted as the Control structure.

2.7 Experimental validation of cellular PLSs through 3D printing

With the aim of designing PLSs with enhanced recovery force, the optimal structures identified in the preceding section are 3D-printed using an open material DLP Addit. Manuf. system (Bison 1000). The printing process operates at a temperature of 40°C,

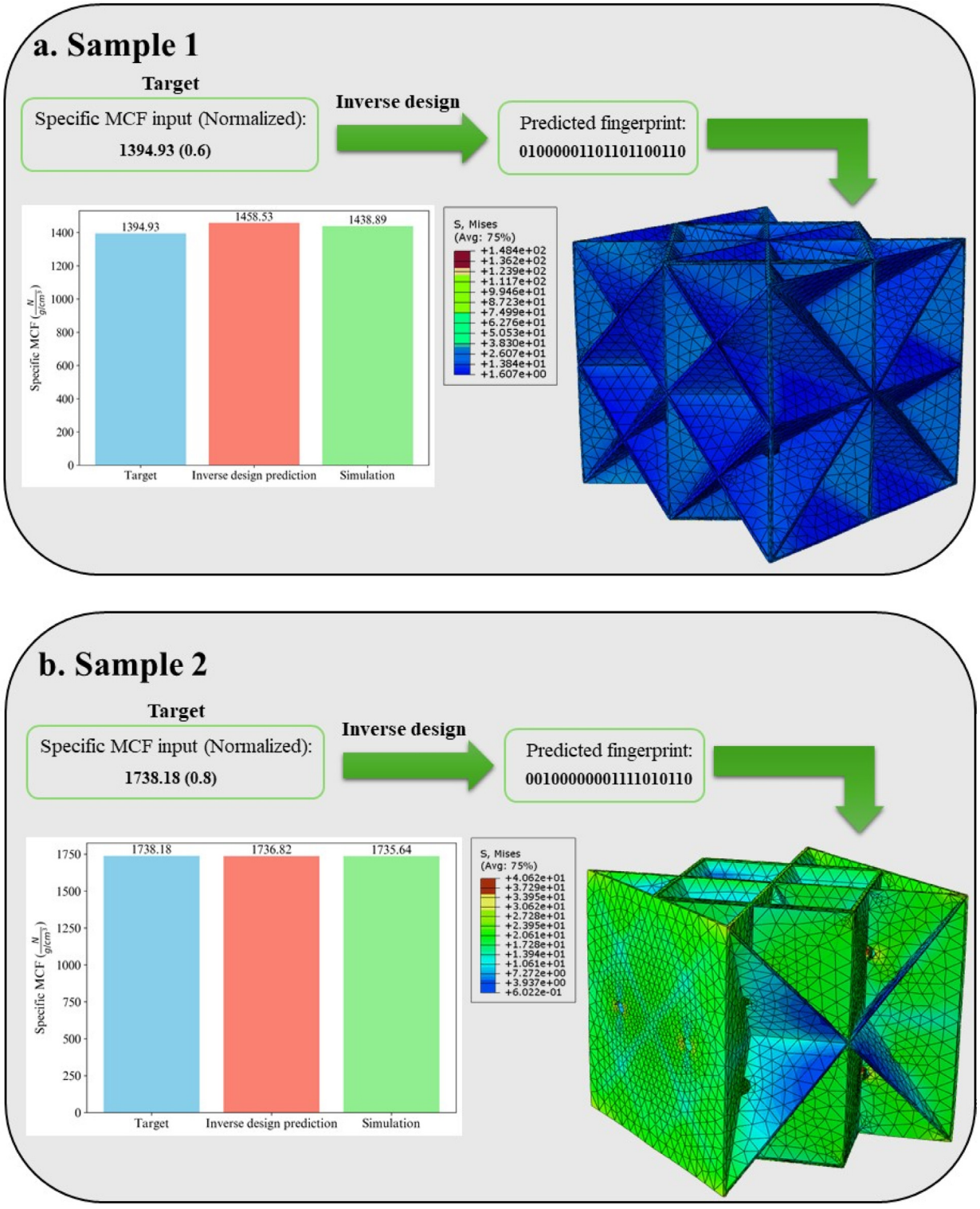

Fig. 8

Numerical validation of the inverse design framework. (a) Sample 1 validation with the fingerprint (01000001101101100110). (b) Sample 2 validation with the fingerprint (00100000001111010110).

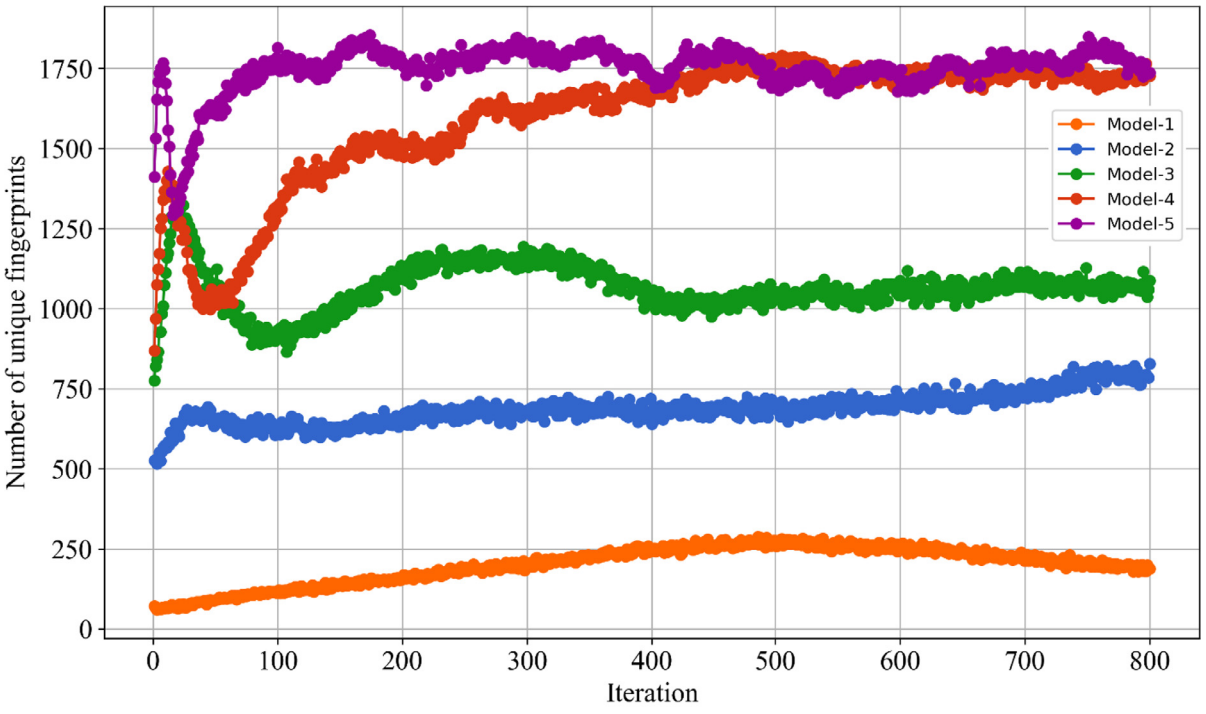

(a)

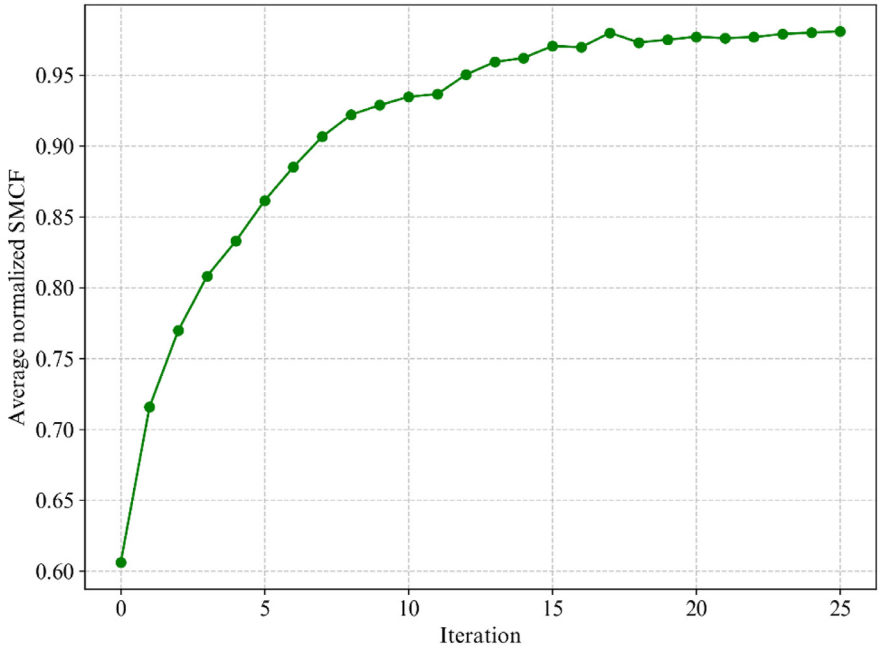

(b)

Fig. 9

(a) The number of unique fingerprints generated by the various models used in the otimization process (b) The average normalized SMCF of the PLSs in each iteration.

and the layer thickness is set at 25 μm. At first, the structures were designed in Abaqus and saved with the STEP format. Then each STL file was imported to Solidworks 2022 and saved as an STL (Stereo Lithography) file. The dimensions of the PLSs were 20×20×20 mm and the thickness of the plates were 0.25, 0.35, 0.45, and 0.55 mm. In order to conduct a performance comparison between the PLSs and the bulk polymer, solid cylinders were fabricated (12.5mm in diameter and 25mm in height) using the 3D printer. The SMP utilized in this investigation is created by blending 60 % Tris[2-(acryloyloxy) ethyl] isocyanurate with 40 % EPON 826 resin. A comprehensive examination, including the synthesis process, thorough characterization, and the outcomes of various tests, will be documented and presented in a forthcoming research paper. After the 3D printing process using the Bison 1000 DLP Addit. Manuf. system, the printed structures, including the PLSs and solid cylinders, underwent a crucial postprocessing phase to enhance their mechanical properties. The postprocessing involved a thorough washing of the 3D-printed objects to remove any residual uncured resin and support material. Subsequently, the samples were subjected to a post-curing process to ensure optimal cross-linking and mechanical strength. This post-curing step typically involves exposing the printed objects to ultraviolet (UV) light for 3min. Both the postprocessing steps have been done in the Anycubic Wash & Cure Plus Machine.

To perform the shape memory programming and force recovery tests, an MTS machine manufactured by ADMET (Model: 1210FHH-2K-B, USA) equipped with a heating chamber is employed. The heating chamber is preheated to approximately 70°C (with the bulk polymer's glass transition temperature being around 65°C) for one hour before the training process. This precaution is implemented to avoid any misleading readings induced by thermal expansions in the fixtures. After the chamber reaches the desired temperature and is prepared, the samples are left to equilibrate inside for 30 minutes to achieve the rubbery state. Afterward, the samples undergo compression programming, reaching a 7.5 % strain at a displacement rate of 0.2 mm/min. Once the specified strain percentage is attained, the specimens are stabilized in their compressed form by rapidly lowering the temperature to room temperature while keeping the strain at a constant level. Upon returning to room temperature, the load is released to stabilize a temporary shape. It is noteworthy that the shape fixity ratio, as defined in Eq. (1), is nearly 100 % for all structures. Subsequently, the recovery force for each sample is measured using the MTS machine. This involves reheating the samples back to 70°C while maintaining the recovery strain at zero.

$$F = \frac{\varepsilon_f}{\varepsilon_l} \times 100\% \quad (1)$$

here, ε_f represents the strain that remains fixed after the load is removed, while ε_l denotes the strain measured before the load is removed.

3 Results

Decision tree analysis was used to quantify the importance of individual walls in a PLS performance, employing binary fingerprints as features. The methodology elucidates critical walls impacting SMCF, providing insights for structural optimization and design decisions. Moreover, the optimum PLSs, which were suggested using the inverse design approach in the preceding sections, were simulated, and additively manufactured for the purpose of numerical and experimental verification. Additionally, shape recovery tests were performed on the optimum structures to compare their performance.

Firstly, we assessed the contribution of each wall and its ability to withstand compressive loads using a Decision Tree Regressor model. Each wall is represented by a binary fingerprint encoding its structural position. The model is trained on a dataset comprising 2000 fingerprints and corresponding SMCF. The feature importance is computed for each wall from the trained model (Fig. 10), revealing the relative contribution of each wall to the overall structural performance.

The resulting feature importance depicts the significance of each wall in a PLS, with higher values indicating greater influence. Specifically, walls 11, 12, 4, and 3 emerge as the most critical components in terms of load tolerance within a PLS. In addition, this result validates the optimization process as the mentioned walls are present in the selected structures. While the Best-1 and Best-2 structures have eight and nine walls in their structures, respectively, all four of the most influential walls are present in both structures.

Fig. 11 illustrates numerical comparisons carried out using the Abaqus simulation tool, in conjunction with experimental validations, for PLSs. In Fig. 11, it is important to highlight that the comparisons were specifically based on the wall thickness of the PLSs. The suggested PLSs can be observed to demonstrate superior relative compression force characteristics when compared to the conventional Control structure. Moreover, the small error between the numerical and experimental results of each PLS indicates the accuracy of the presented FEM model. The incongruence between simulation outcomes and experimental findings can be ascribed to the inherent abstractions in the simulation model, which may oversimplify intricate real-world dynamics. Discrepancies might also arise from variations in boundary conditions, material properties, and the inherent uncertainty in measurement precision during experimental procedures. Results indicate that among the optimum PLSs, the Best-1 structure has the highest SMCF by an average of 79.66 % over all plate thicknesses compared to the Control structure. After that Best-2 and Best-Iso, by an average of 70.55 % and 22.72 %, respectively, have higher SMCF compared to the Control structure.

We would like to further explain the difference between the experimental results and FEM results. In this study, PLS is a very complex structure with many sharp corners and edges, which are the locations for stress and strain concentrations. As a result, although the overall strain applied during the test is within the linear elastic region of the material, local strain concentration cannot be avoided, leading to finite strain in local regions, which may exceed the linear elastic limit and become nonlinear elastic or even plastic. As a result, during the experiment, the material may experience nonlinear behavior, while our FEM only used linear elastic constitutive model, leading to deviation between the experiment and FEM results. As for the reason why the PLS with wall thickness of 0.35 mm has a higher normalized compressive

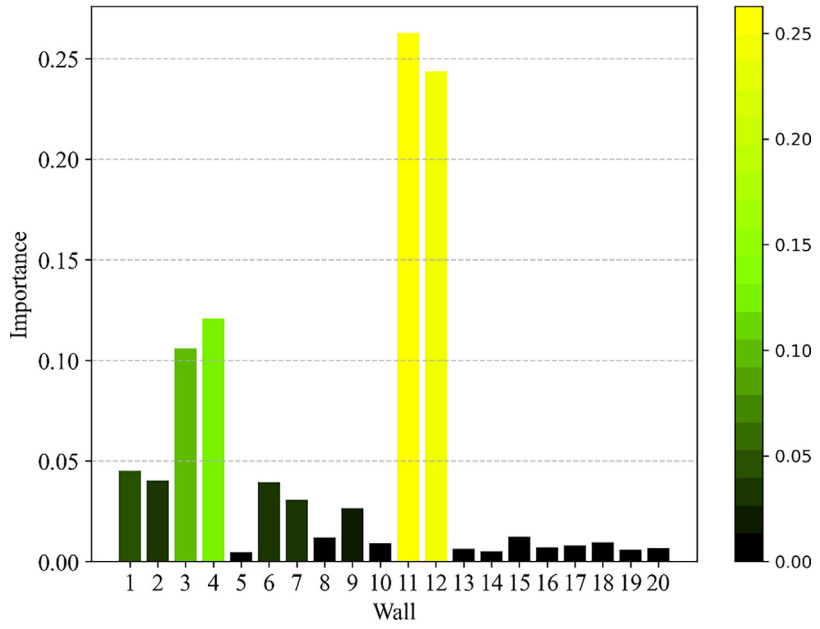

Fig. 10

Relative importance of each wall in specific compressive load tolerance, depicted using a Decision Tree Regressor model.

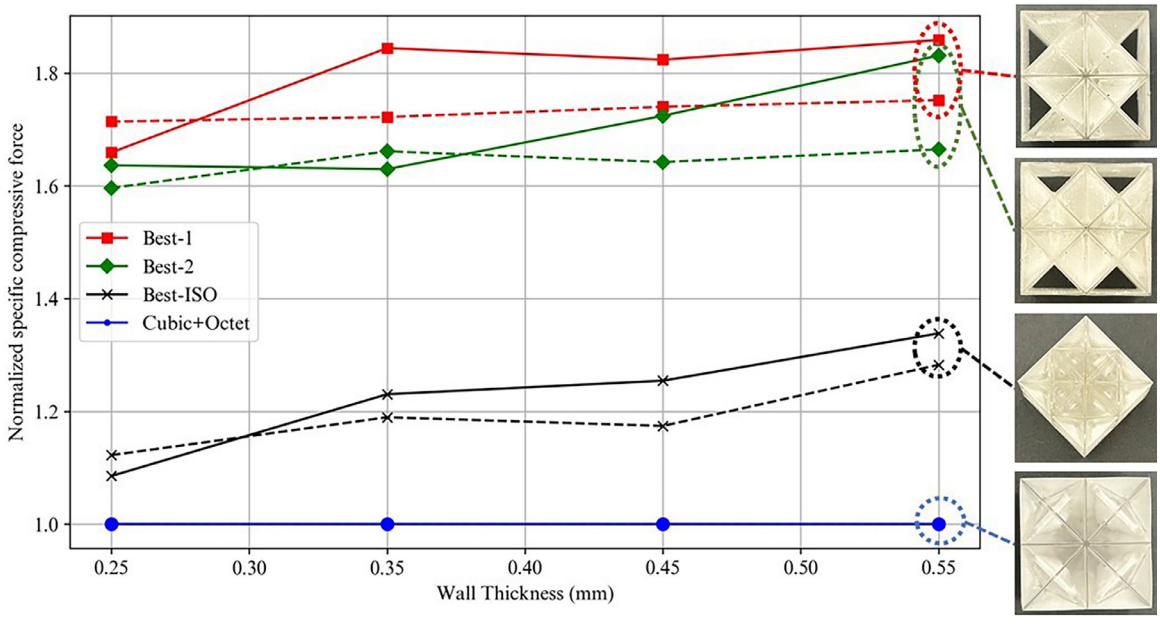

Fig. 11

Comparative analysis between experimental results (indicated by solid lines) and numerical results (represented by dashed lines) for PLSs.

force than the one with 0.45 wall thickness in the FEM, it is likely due to the local stress and strain concentrations in the PLS, leading to complex correlation between the normalized compressive force and the wall thickness. However, as discussed above, our FEM based on linear elasticity cannot capture this nonlinear behavior. This is a very interesting point, which will be a topic for our future studies.

Fig. 12 illustrates the comparisons of the SRF between the optimal PLSs, the Control PLS and the solid cylinder. As depicted in Fig. 12, the optimal PLSs exhibit approximately 30 ∼ 170 % greater SRF (recovery force/density) when compared to the Control PLS with equivalent lattice member thickness. Moreover, while the solid cylinder is performing better than Best-2, Best-Iso, and Control in all wall thicknesses, the Best-1 structure has higher SRF compared to the solid cylinder in 0.45 and 0.55 wall thicknesses by about 12–14 %. Furthermore, this result indicates that for a given volume and mass, the optimum design can produce higher recovery force compared to Control, solid cylinder, and other designs.

Additionally, it is essential to recognize that the optimization process is dependent solely on the structural behavior of the PLSs. It is crucial to acknowledge that utilizing different SMPs can

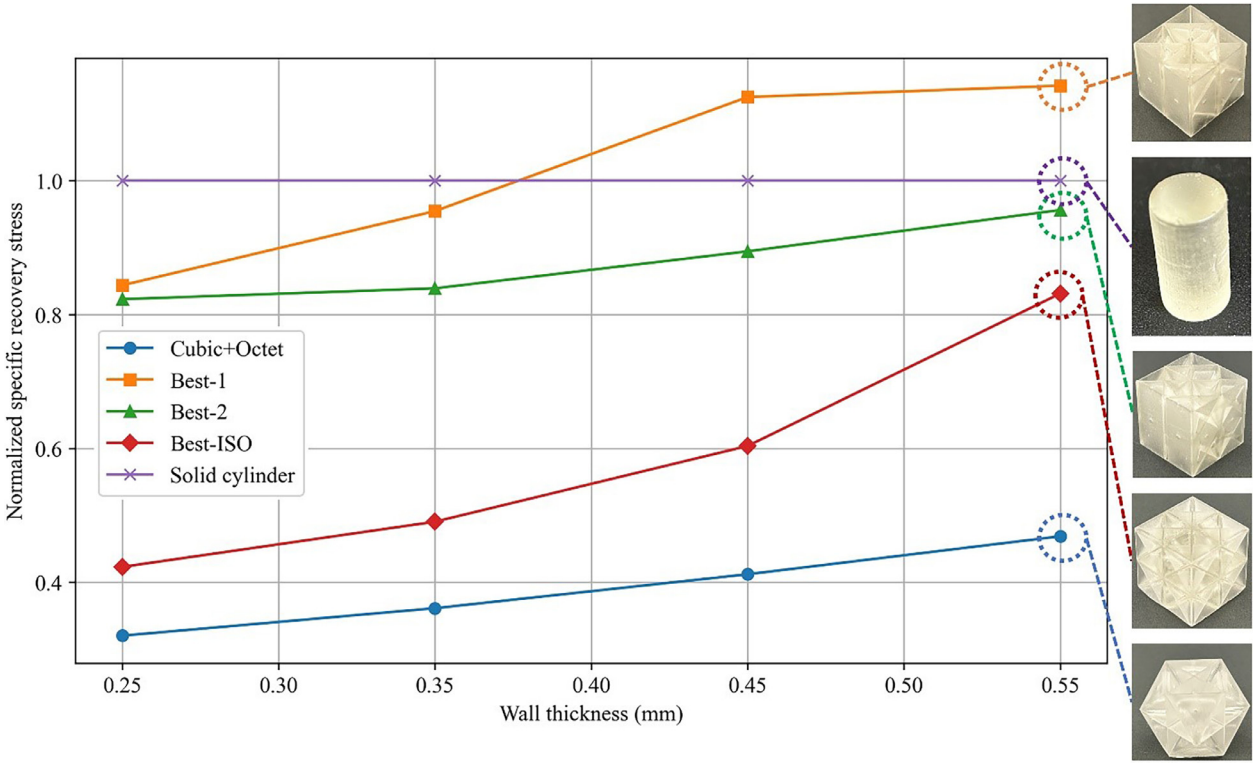

Fig. 12

Experimental comparisons for normalized specific recovery force of PLSs.

influence both structural performance and the manifestation of the shape memory effect. In this study, the selected SMP displays brittleness at room temperature, which could potentially impose constraints on overall displacements before reaching fracture. The utilization of a more ductile SMP has the potential to enhance the extent of displacements during the training or programming of the structures. The observed correlation between higher wall thickness and increased SRF in PLSs is attributed to the greater structural stiffness and enhanced resistance to deformation in structures with thicker walls. The increased thickness contributes to higher energy storage capacity and, consequently, results in a more substantial recovery force during the shape memory effect.

4 Conclusion

The design possibilities in mechanical metamaterials like PLSs are vast. With the advancements in innovative simulation methods, machine learning models, and manufacturing techniques, the transition of these structures into practical applications is becoming significantly more feasible. Despite significant efforts in studying various PLSs and their behaviors, a considerable portion of the design space still awaits exploration.

An Inverse design framework developed to generate PLSs with user-defined SMCF. Several methods implemented to validate the accuracy of the model. Across all input conditions, the average MAE remains stable at 6.72±0.23 % between the target values and the SMCF of the generated fingerprints. Additionally, two samples were generated as case studies for the numerical validation of the framework. Error between the input condition and the SMCF of the generated PLSs were 3.05 % in sample 1 and 0.1 % in sample 2.

Furthermore, this work investigates lightweight PLSs with enhanced shape memory characteristics. A unique approach to design is introduced, utilizing a combination of DNN and GAN models to optimize the recovery force in these metamaterials. Incorporating small 1 mm diameter holes on the surfaces of the plates facilitated the elimination of unpolymerized resin after the printing process, even in the presence of a closed-cell topology. The accuracy of the predicted unit cells is confirmed through both numerical simulations and experimental testing, demonstrating a performance improvement ranging from 22.7 % to 79.6 % compared to the Control PLS when subjected to uniaxial compression. We also studied the recovery force of the optimized structures and compared them with those of the Control PLS and a solid cylinder. The findings suggest that the optimal PLSs display an SFR (recovery force/density) approximately 30 ~ 170 % higher than that of the Control PLS with the same lattice member thickness. Furthermore, while the solid cylinder outperforms Best-2, Best-Iso, and Control across all wall thicknesses, the Best-1 structure exhibits a higher recovery force than the solid cylinder by approximately 12-14 % at wall thicknesses of 0.45 and 0.55. An aspect of the inverse machine learning framework is its capability to continually optimize PLSs. This is achieved through iterative processes, wherein the newly generated PLSs are employed as a training dataset for predicting the next generation of designs. The application of this framework extends beyond optimizing PLSs and can be employed for enhancing other forms of structural design. It enables the generation of novel

structures tailored to specific mechanical property ranges. Given the outstanding performance of the optimized plate-lattice unit cells and the reliable prediction accuracy of the DNNs and inverse design framework, it is evident that this technique is versatile enough to be utilized in the design and optimization of various metamaterials, including those geared towards impact absorption, increased deformation or buckling strengths, and shape recovery.

Contributions

A.T. contributed towards design of work, data generation, design and analysis and wrote the manuscript. A.C. contributed towards design and analysis. J.K. helped in preparing the 3D printable SMP. G.L. initiated the conception, raised funding for the work, guided the research, and co-wrote the manuscript.

Supporting information

All other data are available from the authors upon reasonable request.

Declaration of competing interest

The authors declare no conflict of interest.

Data availability

Data will be made available on request.

CRediT authorship contribution statement

Amir Teimouri: Writing – original draft, Visualization, Software, Methodology, Investigation, Formal analysis, Data curation, Conceptualization. **Adithya Challapalli:** Software, Data curation. **John Konlan:** Investigation, Data curation. **Guoqiang Li:** Writing – review & editing, Supervision, Resources, Project administration, Funding acquisition, Conceptualization.

Acknowledgements

This work is supported by the US National Science Foundation under Grant Number OIA-1946231 and the Louisiana Board of Regents for the Louisiana Materials Design Alliance (LAMDA), and National Science Foundation under grant number 1736136.

Supplementary materials

Supplementary material associated with this article can be found, in the online version, at doi:10.1016/j.giant.2024.100282.

References

[1] F Momeni, X Liu, J. Ni, A review of 4D printing, Mater. Design 122 (2017) 42–79.

[2] A Sydney Gladman, EA Matsumoto, RG Nuzzo, L Mahadevan, JA Lewis, Biomimetic 4D printing, Nat. Mater. 15 (4) (2016) 413–418.

[3] G Stoychev, A Kirillova, L. Ionov, Light-responsive shape-changing polymers, Adv. Opt. Mater. 7 (16) (2019) 1900067.

[4] L Hu, Y Wan, Q Zhang, MJ. Serpe, Harnessing the power of stimuli-responsive polymers for actuation, Adv. Funct. Mater. 30 (2) (2020) 1903471.

[5] Y Liu, H Lv, X Lan, J Leng, S Du, Review of electro-active shape-memory polymer composite, Compos. Sci. Technol. 69 (13) (2009) 2064–2068.

[6] H Meng, G. Li, A review of stimuli-responsive shape memory polymer composites, Polymer 54 (9) (2013) 2199–2221.

[7] G Li, D. Nettles, Thermomechanical characterization of a shape memory polymer based self-repairing syntactic foam, Polymer 51 (3) (2010) 755–762.

[8] S Sarrafan, G. Li, Conductive and ferromagnetic syntactic foam with shape memory and self-healing/recycling capabilities, Adv. Funct. Mater. 34 (11) (2024) 2308085.

[9] W Zhao, C Yue, L Liu, Y Liu, J. Leng, Research progress of shape memory polymer and 4D printing in biomedical application, Adv. Healthcare Mater. 12 (16) (2023) 2201975.

[10] Y Liu, H Du, L Liu, L. Leng, Shape memory polymers and their composites in aerospace applications: a review, Smart Mater. Struct. 23 (2) (2014) 023001.

[11] B Jin, H Song, R Jiang, J Song, Q Zhao, T. Xie, Programming a crystalline shape memory polymer network with thermo-and photo-reversible bonds toward a single-component soft robot, Sci. Adv. 4 (1) (2018) eaao3865.

[12] S Miao, N Castro, M Nowicki, L Xia, H Cui, X Zhou, et al., 4D printing of polymeric materials for tissue and organ regeneration, Mater. Today 20 (10) (2017) 577–591.

[13] J Fan, G. Li, High performance and tunable artificial muscle based on two-way shape memory polymer, RSC Adv. 7 (2) (2017) 1127–1136.

[14] G Li, T. Xu, Thermomechanical characterization of shape memory polymer–based self-healing syntactic foam sealant for expansion joints, J. Transp. Eng. 137 (11) (2011) 805–814.

[15] A Mansour, A Dahi Taleghani, S Salehi, G Li, C Ezeakacha, Smart lost circulation materials for productive zones, J. Petroleum Explor. Product. Technol. 9 (2019) 281–296.

[16] J Mendez, PK Annamalai, SJ Eichhorn, R Rusli, SJ Rowan, EJ Foster, et al., Bioinspired mechanically adaptive polymer nanocomposites with water-activated shape-memory effect, Macromolecules 44 (17) (2011) 6827–6835.

[17] M Mattmann, C De Marco, F Briatico, S Tagliabue, A Colusso, XZ Chen, et al., Thermoset shape memory polymer variable stiffness 4D robotic catheters, Adv. Sci. 9 (1) (2022) 2103277.

[18] Q Ze, X Kuang, S Wu, J Wong, SM Montgomery, R Zhang, et al., Magnetic shape memory polymers with integrated multifunctional shape manipulation, Adv. Mater. 32 (4) (2020) 1906657.

[19] TT Nguyen, J. Kim, 4D-printing—Fused deposition modeling printing and PolyJet printing with shape memory polymers composite, Fibers Polym. 21 (2020) 2364–2372.

[20] C Crook, J Bauer, A Guell Izard, C Santos de Oliveira, J Martins de Souza e Silva, JB Berger, et al., Plate-nanolattices at the theoretical limit of stiffness and strength, Nat. Commun. 11 (1) (2020) 1579.

[21] A Challapalli, G. Li, 3D printable biomimetic rod with superior buckling resistance designed by machine learning, Sci. Rep. 10 (1) (2020) 20716.

[22] N Korshunova, G Alaimo, SB Hosseini, M Carraturo, A Reali, J Niiranen, et al., Image-based numerical characterization and experimental validation of tensile behavior of octet-truss lattice structures, Addit. Manuf. 41 (2021) 101949.

[23] SC Han, JW Lee, K. Kang, A new type of low density material: Shellular, Adv. Mater. 27 (37) (2015) 5506–5511.

[24] J Berger, H Wadley, R. McMeeking, Mechanical metamaterials at the theoretical limit of isotropic elastic stiffness, Nature 543 (7646) (2017) 533–537.

[25] O Sigmund, N Aage, E. Andreassen, On the (non-) optimality of Michell structures, Struct. Multidiscip. Optim. 54 (2016) 361–373.

[26] Y. Liu, Mechanical properties of a new type of plate–lattice structures, Int. J. Mech. Sci. 192 (2021) 106141.

[27] T Tancogne-Dejean, M Diamantopoulou, MB Gorji, C Bonatti, D. Mohr, 3D plate-lattices: an emerging class of low-density metamaterial exhibiting optimal isotropic stiffness, Adv. Mater. 30 (45) (2018) 1803334.

[28] S Kamarian, A Khalvandi, E Heidarizadi, S Saber-Samandari, J-i. Song, Prediction and optimization of 3D-printed sandwich beams with chiral cores, Int. J. Mech. Sci. 262 (2024) 108747.

[29] J Huo, Y Wang, N Wang, W Gao, J Zhou, Y. Cao, Data-driven design and optimization of ultra-tunable acoustic metamaterials, Smart Mater. Struct. 32 (5) (2023) 05LT1.

[30] S Saurabh, A Gupta, R. Chowdhury, Impact of parametric variation to achieve extreme mechanical metamaterials through topology optimization, Compos. Struct. 326 (2023) 117611.

[31] F Dos Reis, N Karathanasopoulos, Inverse metamaterial design combining genetic algorithms with asymptotic homogenization schemes, Int. J. Solids Struct. 250 (2022) 111702.

[32] Y Noguchi, T Yamamoto, K Matsushima, T. Yamada, Labyrinthine acoustic metamaterials with a subwavelength bandgap inspired by topology-optimized structural design, Adv. Eng. Mater. 25 (4) (2023) 2201104.

[33] X Fang, H-S Shen, H. Wang, Diverse 3D auxetic unit cell inverse design with deep learning, Appl. Phys. Rev. 10 (3) (2023).

[34] JK Wilt, C Yang, GX. Gu, Accelerating auxetic metamaterial design with deep learning, Adv. Eng. Mater. 22 (5) (2020) 1901266.

[35] X Zheng, T-T Chen, X Guo, S Samitsu, I. Watanabe, Controllable inverse design of auxetic metamaterials using deep learning, Materi. Design 211 (2021) 110178.

[36] M Lei, W Hong, Z Zhao, C Hamel, M Chen, H Lu, et al., 3D printing of auxetic metamaterials with digitally reprogrammable shape, ACS Appl. Mater. Interfaces 11 (25) (2019) 22768–22776.

[37] C Yan, X Lin, X Feng, H Yang, P Mensah, G. Li, Advancing flame retardant prediction: A self-enforcing machine learning approach for small datasets, Appl. Phys. Lett. 122 (25) (2023).

[38] C Yan, X Feng, G. Li, From drug molecules to thermoset shape memory polymers: a machine learning approach, ACS Appl. Mater. Interfaces 13 (50) (2021) 60508–60521.

[39] A Challapalli, J Konlan, D Patel, G. Li, Discovery of cellular unit cells with high natural frequency and energy absorption capabilities by an inverse machine learning framework, Front. Mech. Eng. 7 (2021) 779098.

[40] G Moon, J-r Choi, C Lee, Y Oh, KH Kim, D. Kim, Machine learning-based design of meta-plasmonic biosensors with negative index metamaterials, Biosens. Bioelectron. 164 (2020) 112335.

[41] F Liu, X Jiang, X Wang, L. Wang, Machine learning-based design and optimization of curved beams for multistable structures and metamaterials, Extreme Mech. Lett. 41 (2020) 101002.

[42] AP Garland, BC White, SC Jensen, BL. Boyce, Pragmatic generative optimization of novel structural lattice metamaterials with machine learning, Mater. Design 203 (2021) 109632.

[43] A Challapalli, J Konlan, G. Li, Inverse machine learning discovered metamaterials with record high recovery stress, Int. J. Mech. Sci. 244 (2023) 108029.

[44] S Van't Sant, P Thakolkaran, J Martínez, S. Kumar, Inverse-designed growth-based cellular metamaterials, Mech. Mater. 182 (2023) 104668.

[45] A Challapalli, G. Li, Machine learning assisted design of new lattice core for sandwich structures with superior load carrying capacity, Sci. Rep. 11 (1) (2021) 18552.

[46] A Challapalli, D Patel, G. Li, Inverse machine learning framework for optimizing lightweight metamaterials, Mater. Design 208 (2021) 109937.

[47] J Fan, G. Li, High enthalpy storage thermoset network with giant stress and energy output in rubbery state, Nat. Commun. 9 (1) (2018) 642.

[48] M. Shema, Seven deadliest web application attacks, Syngress, 2010.

[49] M Hossain, Z. Liao, An additively manufactured silicone polymer: thermo-viscoelastic experimental study and computational modelling, Addit. Manuf. 35 (2020) 101395.

[50] DS Ibarra, J Mathews, F Li, H Lu, G Li, J. Chen, Deep learning for predicting the thermomechanical behavior of shape memory polymers, Polymer 261 (2022) 125395.

[51] Holthusen H, Lamm L, Brepols T, Reese S, Kuhl E. Theory and implementation of inelastic Constitutive Artificial Neural Networks. arXiv preprint arXiv:231106380. 2023.

[52] F As'ad, C. Farhat, A mechanics-informed deep learning framework for data-driven nonlinear viscoelasticity, Comput. Methods Appl. Mech. Eng. A 417 (2023) 116463.

[53] NG Morales, TJ Fleck, JF. Rhoads, The effect of interlayer cooling on the mechanical properties of components printed via fused deposition, Addit. Manuf. 24 (2018) 243–248.

[54] A Gulli, S. Pal, Deep learning with Keras, Packt Publishing Ltd, 2017.

[55] A. Borji, Pros and cons of GAN evaluation measures: new developments, Comput. Vision Image Understanding 215 (2022) 103329.